

Optics Letters

Dissipative Kerr solitons, breathers, and chimera states in coherently driven passive cavities with parabolic potential

YIFAN SUN,^{1,*†} PEDRO PARRA-RIVAS,^{1,†} MARIO FERRARO,¹ FABIO MANGINI,¹ MARIO ZITELLI,¹ RAPHAËL JAUBERTEAU,¹ FRANCESCO RINALDO TALENTI,¹ AND STEFAN WABNITZ^{1,2}

¹Department of Information Engineering, Electronics and Telecommunications, Sapienza University of Rome, Via Eudossiana 18, 00184 Rome, Italy

²CNR-INO, Istituto Nazionale di Ottica, Via Campi Flegrei 34, 80078 Pozzuoli, Italy

*Corresponding author: yifan.sun@uniroma1.it

†These authors contributed equally to this work.

Received 17 August 2022; revised 7 November 2022; accepted 12 November 2022; posted 14 November 2022; published 7 December 2022

We analyze the stability and dynamics of dissipative Kerr solitons (DKSs) in the presence of a parabolic potential. This potential stabilizes oscillatory and chaotic regimes, favoring the generation of static DKSs. Furthermore, the potential induces the emergence of new dissipative structures, such as asymmetric breathers and chimera-like states. Based on a mode decomposition of these states, we unveil the underlying modal interactions. © 2022 Optica Publishing Group

<https://doi.org/10.1364/OL.472900>

Dissipative temporal Kerr soliton (DKS) [1] generation and manipulation have been an emerging topic in photonics over the past decade, since they provide a breakthrough framework for coherent frequency comb generation in chip-scale microresonator platforms [2,3]. In contrast to conservative systems, where solitons are formed due to a counter-balance between dispersion and nonlinearity, dissipative solitons additionally require an equilibrium between internal dissipation and external energy flow or driving. The dynamics and stability of DKSs have been analyzed in detail in the mean-field approximation, where passive Kerr resonators are described by a driven and damped nonlinear Schrödinger model [4,5]. In this context, a large variety of DKSs emerge in anomalous and normal dispersion regimes [6–8]. As the pump intensity grows larger, DKSs undergo different types of instabilities, leading to complex spatiotemporal dynamics, which can be either periodic (i.e., breathers) or chaotic [9–13].

Spatiotemporal dynamics can be stabilized through high-order effects, such as third-order dispersion, which considerably reduces the extension of unstable parameter regions in favor of static DKSs [14,15]. Moreover, third- and fourth-order dispersion effects may lead to the appearance of new types of localized states, and to the coexistence of bright and dark DKSs [16–18], as it also does the Raman effect [19]. Spatiotemporal instabilities may also be suppressed by the modulation of the intracavity background field. These modulated defects can be induced through the external phase of the driving

field [20–25], or by synchronous intracavity phase modulation [26,27]. The latter can be introduced via an electrooptic modulator, and it leads to a synthetic dimension [27,28]. Both methods create an effective periodic potential, which provides an additional degree of freedom for controlling spatiotemporal dynamics and emerging states. Together with the stabilization of chaotic states [29], the potential may lead to the emergence of chimera-like states [28,30]. Furthermore, a modulated background provides different advantages, such as enhancing the pump-to-soliton conversion efficiency [25], and providing additional deterministic routes for DKSs generation, without undergoing a spatiotemporal chaotic phase [31].

In this Letter, we theoretically show that a parabolic potential in time plays a key role on the stability of DKSs and other spatiotemporal dissipative structures emerging in a dispersive Kerr resonator with anomalous dispersion. The parabolic potential approximates a periodic (e.g., sinusoidal) potential around the center of the DKS. Specifically, we find that, for low pump values, the potential stabilizes oscillatory and chaotic dynamics in favor of static DKS. As the pump power grows larger, the potential induces the appearance of asymmetric breathers and chaoticons (i.e., chimera-like states) [32], where the background field state coexists with a spatiotemporal localized chaotic state. Moreover, chaoticons coexist with single-peak DKSs, and form a hysteresis loop. To support our findings, we carry out a systematic bifurcation analysis, which establishes the connection with the multimodal structure of the potential.

In the mean-field approximation, the coherently driven and phase modulated passive cavity is described by the equation

$$\partial_t A = i\partial_\tau^2 A - iC\tau^2 A + i|A|^2 A - (1 + i\delta)A + P, \quad (1)$$

where $A(\tau, t)$ is the slowly varying envelope of electric field, and τ, t are the fast and slow time, respectively [4]. The term ∂_τ^2 is second-order anomalous chromatic dispersion, δ is the phase detuning, P is the driving pump field amplitude, and the linear loss coefficient, without loss of generality, is normalized to 1. We introduce the parabolic temporal potential $C\tau^2$, where C controls

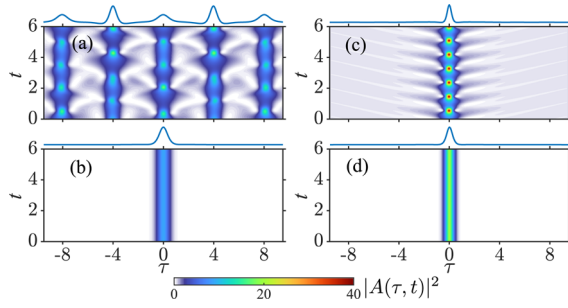


Fig. 1. (a),(c) Comparison of solutions without the potential $C = 0$ and (b),(d) with the potential $C = 1$, when the parameters are (a),(b) $P = 2.5$, $\delta = 3$ and (c),(d) $P = 4.5$, $\delta = 8$.

its curvature. Note that such type of potential describes a trap in Bose–Einstein condensates, and a transverse index profile in graded-index multimode fibers [33]. With the usual change of the meaning of the coordinates (e.g., modify time τ with space x), Eq. (1) also describes the spatial dynamics of one-dimensional (e.g., consider slab waveguides) driven nonlinear passive cavities with a graded refractive index [34]. To study the dynamics of Eq. (1), we perform both direct numerical simulations (DNSs) with a pseudospectral method, and numerical path-continuation of the stationary solutions A_s (i.e., $\partial_t A_s = 0$) by using AUTO-07p [35]. The latter allows us to compute both stable and unstable steady-state solutions, which are not accessible otherwise.

Figures 1(a) and 1(b) show the dynamics of solutions of Eq. (1) in the absence of the potential ($C = 0$). The temporal evolution $[|A(\tau)|^2]$ versus t of a chaotic Turing pattern, and its final state are shown in Fig. 1(a) for $(P, \delta) = (2.5, 3)$. Whereas, Fig. 1(c) shows a breather DKS for $(P, \delta) = (4.5, 8)$. For this set of parameters, static DKSs are always unstable [36]. When the potential is introduced ($C = 1$) [see Figs. 1(b) and 1(d)], these dynamics are stabilized, leading to stationary DKSs.

In order to understand the mechanism for this stabilization, we perform a bifurcation analysis of the DKSs, with and without a temporal potential. These results are illustrated in Fig. 2, using $I_{\text{center}} \equiv |A(0)|^2$ versus δ . We set $P = 2.5$ in Figs. 2(a) and 2(b), $P = 4.5$ in Figs. 2(c) and 2(d), $C = 0$ in Figs. 2(a) and 2(c), and $C = 1$ in Figs. 2(b) and 2(d). Stable and unstable steady-state branches are computed by path-continuation algorithms; dynamical states are calculated by DNSs.

Figure 2(a) shows the bifurcation diagram in the absence of potential, with $P = 2.5$. The blue curve corresponds to the continuous-wave (CW) state of Eq. (1). The CW state is stable until the saddle-node (SN) bifurcation SN_h^l , where it becomes unstable (see dashed blue lines). The DKS bifurcates from SN_h^l with a small amplitude, and it remains unstable (see orange dashed lines) [7]. By increasing δ , the DKS eventually stabilizes at SN_r^l , and it retains stability until reaching SN_l^l (see solid red line). These solitons have a non-zero background (corresponding to the CW state), and their localized profile can be approximated by a sech-shape [1]. When decreasing δ below SN_h^l , the DKS background becomes unstable, leading to chaotic Turing pattern states, such as in the example shown in Fig. 1 for $(\delta, P) = (3, 2.5)$. The peak intensity values of these states are plotted by gray dots in Fig. 2(a).

This scenario drastically changes in the presence of the parabolic potential [see Fig. 2(b)]. Now, the CW state diagram merges with the solution branches corresponding to the DKS, leading to the single curve of Fig. 2(b). Each branch on this curve

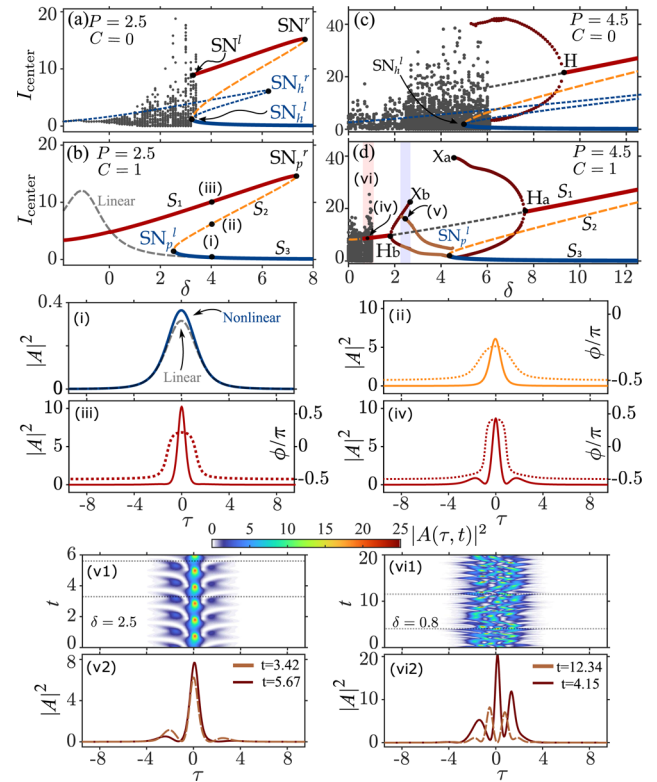


Fig. 2. Bifurcation diagrams showing I_{center} versus δ for (a) $(P, C) = (2.5, 0)$, (b) $(P, C) = (2.5, 1)$, (c) $(P, C) = (4.5, 0)$, and (d) $(P, C) = (4.5, 1)$. The dashed gray line in (b) is the linear steady-state solution, to be compared with the nonlinear solution. Panels (i)–(iii) show the intensity $|A|^2$ (solid line) and phase ϕ (dashed line) of the three localized solutions S_1 , S_2 , and S_3 , corresponding to the curves in panels (b),(d); panel (iv) corresponds to the DKS solution in panel (d). Panel (v1) shows the evolution of a τ -asymmetric state for $\delta = 2.5$; panel (vi1) shows a chaotic state for $\delta = 0.8$, corresponding to panel (d). (See Visualization 1 and Visualization 2.) We plot the corresponding field powers at different slow times in panels (v2) and (vi2), respectively.

corresponds to a localized state, as depicted in Figs. 2(i)–2(iii), and branches are interconnected through the SN bifurcations SN_p^{lr} .

The S_3 state plotted in Fig. 2(i) is a small-amplitude localized pulse, which corresponds to the deformation of the CW state, owing to the presence of the potential. This state extends until SN_p^l , where it connects to the unstable state S_2 [see Fig. 2(ii)]. At SN_p^l , the latter leads to the DKS state S_1 [see Fig. 2(iii)]. Then S_1 rests on the basal state S_3 , and is asymptotically connected to a zero intensity background. For $C = 1$, S_1 extends to negative δ and it is stable. Between SN_p^l and SN_p^r , the localized states S_1 and S_3 coexist for the same range of parameters, and are both stable. They can be easily excited by a Gaussian function of the form $A(\tau) = h \exp(-(\tau/r)^2/2)$, with h and r taking different values. In the absence of nonlinearity, bistability disappears: the linear resonance of Eq. (1) is shown by the dashed gray line in Fig. 2(b). The linear solution, obtained by removing the Kerr term, is also plotted in Fig. 2(i). Therefore, the solution branch S_3 represents a nonlinear deformation of the linear steady-state solution.

As we have anticipated with Fig. 1, the stabilization of the dynamics of solutions to Eq. (1) occurs for different values of

P . To support this, we computed the bifurcation diagram associated with a single-peak soliton for $P = 4.5$, with and without the potential. This situation is depicted in Figs. 2(c) and 2(d). Figure 2(c) shows the bifurcation diagram for $C = 0$. By increasing P , the role of nonlinearity grows larger, which further tilts the resonance (see the blue lines). The DKS solution branches preserve the morphology depicted in Fig. 2(a), although now their range of existence has increased. In this regime, the top DKSs branch undergoes a Hopf bifurcation (H), where the soliton becomes unstable in favor of breathing states. The minimal and maximal value of I_{center} of these breathers are plotted using of brown dots. These breather states are similar to that depicted in Fig. 1(c), and their oscillation amplitude grows larger with decreasing values of δ . Eventually, when SN_h^I is crossed, the stable CW state disappears, and spatiotemporal chaos (STC) develops. Note that STC extends the breather over SN_h^I , and coexists with DKSs or breathers [see Figs. 2(a) and 2(c)].

For $C = 1$ [see Fig. 2(d)], STC is suppressed by the potential, in favor of either static DKS or regular oscillatory states. The DKS S_1 enlarges its stability region, which now extends to H_a , where $\delta_{H_a} \ll \delta_H$. Once H_a is crossed, a τ -symmetric breather arises supercritically, and it increases its oscillation amplitude with decreasing values of δ . Eventually, this stable breather disappears, possibly in a fold of cycles at X_a . By decreasing δ below this point, the system develops τ -asymmetric breathers, such as the one which is depicted in Fig. 2(v) for $(\delta, P) = (2.5, 4.5)$. A special feature of these states is the different evolution of their leading and trailing tails (see Visualization 1). The extrema of these states, at $\tau = 0$, are depicted by using brown dots in Fig. 2(d). Decreasing δ further, the asymmetric breather branch meets with a symmetric one (see dark red branch) and disappears. On the right-hand side, the latter persists until reaching X_b . On the left-hand side, the τ -symmetric breather decreases its amplitude, until it dies out at the Hopf bifurcation H_b . Note the presence of a bistability region between the symmetric and asymmetric breathers [see the light blue shaded area in Fig. 2(d)]. For $\delta < \delta_{H_b}$, DKSs exist [such as the one shown in Fig. 2(iv)], although they lose stability once more around $\delta \approx 0.5$. After this, the solution of Eq. (1) evolves into a very complex spatiotemporal state, such as the one shown in Fig. 2(vi). It consists of a portion of STC which is localized around the center of the temporal domain, owing to the presence of the potential which acts as a trap, thus confining the STCs. Such a type of chaotic pulse was named chaoticon by Vershueren *et al.* [32], although it is also known as chimera state in other works [28,30]. Chaoticons and DKSs [see, respectively, Fig. 2(vi) and Fig. 2(iv) and Visualization 2] coexist within a given δ -range [see the pink shaded area in Fig. 2(d)].

The previously described states can be analyzed in terms of a mode decomposition method. The parabolic potential introduces boundary conditions for the fields, which translate in a finite number of eigenmodes. Therefore, solutions of Eq. (1) in Fig. 2 can be decomposed and analyzed in terms of linear eigenmodes. This provides essential information regarding the underlying nonlinear mode interactions and the global dynamics of Eq. (1). The linear eigenmodes obey the equation

$$\partial_t A = i\partial_\tau^2 A - iC\tau^2 A, \quad (2)$$

which also describes a quantum mechanical harmonic oscillator. Note that a similar equation was also used for describing the dynamics of mode-locked nanolasers [37,38]. As is well known, the eigenmodes of Eq. (2) are the Hermite–Gaussian

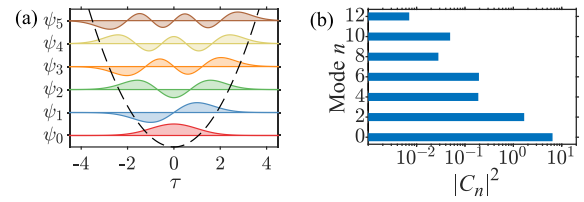


Fig. 3. (a) First six HG linear modes ψ_0, \dots, ψ_5 of Eq. (1) and the parabolic potential (see dashed line), for comparison. (b) Mode energy distribution associated with the S_1 DKS shown in Fig. 2(iii) for $(\delta, P) = (4, 2.5)$, where $|C_n|^2$ represents the energy of the mode n .

(HG) family. The lowest-order six modes are plotted in Fig. 3(a). The neglected terms in Eq. (2), compared with Eq. (1), can be considered as small perturbations. The field envelope $A(\tau, t)$ can be written as a linear superposition of HG modes $\psi_n(\tau)$ with equally spaced frequencies $2\sqrt{C}(n+1/2)$: $A(\tau, t) = \sum_{n=0}^N C_n(t)\psi_n(\tau)$, with N being the total number of modes considered in the analysis. The mode coefficients are computed by projecting any solution on the linear modes, and read as $C_n(t) = \int_{-\infty}^{\infty} A(\tau, t)\psi_n(\tau)d\tau = |C_n(t)| \exp i\phi_n(t)$, where $|C_n(t)|^2$ represents the energy of mode n at time t , and $\phi_n(t)$ is its phase. In Fig. 3(b), we plot the mode energy $|C_n|^2$ distribution associated with the DKS state S_1 in Fig. 2(iii). Note that the energies of asymmetric modes ($n = 1, 3, 5, \dots$) are zero, because the state has a symmetric temporal distribution. Also, S_2 and S_3 have a similar mode distribution (not shown here).

The bifurcation structure shown in Fig. 2(d) ($P = 4.5$) can be revisited by projecting the different DKS branches on HG modes. This projection is depicted in Fig. 4(a), where we plot the mode energy $|C_0|^2$ and $|C_2|^2$ versus δ . Following this diagram, we can

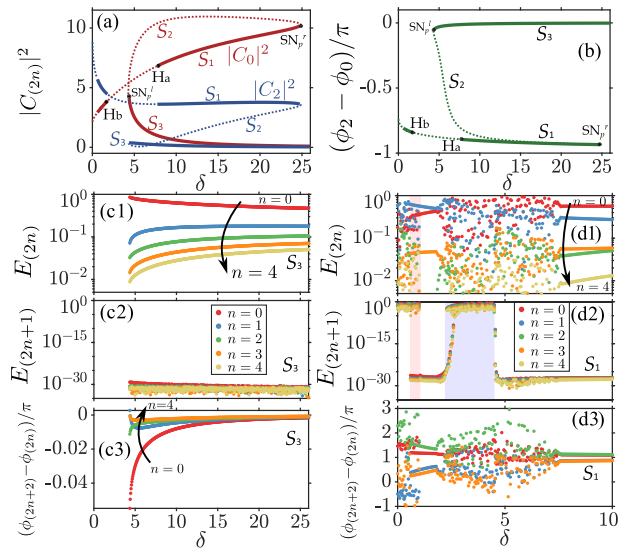


Fig. 4. Mode decomposition of the solutions in Fig. 2(d). (a) Mode energies $|C_0|^2$, $|C_2|^2$ and (b) their phase difference as a function of δ , where solid (dashed) lines represent stable (unstable) solutions. The three subpanels in (c) plot the normalized energies of even modes $E(2n) = |C(2n)|^2/\sum |C(n)|^2$, odd modes $E(2n+1)$, and their phase difference $(\phi_{(2n+2)} - \phi_{(2n)})/\pi$ versus δ , for S_3 solutions in Fig. 2(d). The same quantities of the solutions S_1 of Fig. 2(d) are shown in three subpanels in (d). Chaoticon/DKSs coexistence (asymmetric breathers) is represented by a pink (blue) shaded area.

see how the $\psi_{0,2}$ -mode composition varies along the solution branches S_1 , S_2 , and S_3 .

Interestingly, we found that S_1 and S_3 represent mode-locked states. This is shown in Fig. 4(b), where we show the phase difference between modes ψ_0 and ψ_2 along the bifurcation diagrams of Fig. 4(a). The phase difference between adjacent symmetric modes is $-\pi$ in S_1 (other higher-order modes are not shown here): these modes are locked in anti-phase, in contrast with the in-phase mode locking that occurs for S_3 states. Whereas unstable states S_2 undergo large phase changes between the two modes. Useful insight in the localized states S_1 and S_3 is gained by analyzing the variation of their mode components with cavity detuning δ . For the S_3 branch, the energy fraction of higher-order modes $E_{(2n)} = |C_{(2n)}|^2 / \sum |C_{(n)}|^2$ grows larger as δ increases [see Fig. 4(c1)]. This leads to temporal broadening of the S_3 states, because of the longer temporal duration of higher-order modes. On the other hand, for S_1 the fundamental mode energy $|C_0|^2$ grows significantly larger with δ [see Fig. 4(a)]. This results in a cavity soliton with progressively higher intensity and narrower temporal duration. For both states, the phase difference between adjacent even modes approaches zero when δ increases [see Fig. 4(c3) and Fig. 4(d3)]. This shows that stronger locking occurs for these modes with increasing δ . Furthermore, the mode decomposition analysis allows for making a clear distinction among the symmetric and asymmetric breathers, and chaoticons. In the symmetric breather regime ($1.8 < \delta < 7.5$), only even mode energies [see Fig. 4(d1)] and phase differences [see Fig. 4(d3)] fluctuate. This is in contrast with the case of asymmetric breathers, which exhibits significant odd mode components [see Fig. 4(d2)]. These odd modes contribute to the asymmetric breather evolution. When compared with asymmetric breathers, chaoticons exhibit much wider phase fluctuations [see Fig. 4(d3)].

In summary, by applying a bifurcation analysis, we revealed the emergence and stability of dissipative states for a coherently driven, passive nonlinear and dispersive cavity with a parabolic potential. The potential may stabilize complex spatiotemporal dynamics in favor of static DKSSs, and leads to the coexistence of high- and low-amplitude localized states. A particular feature of this system is that asymmetric breathers and chimera-like states (i.e., a chaoticons) may arise. The latter consist of localized spatiotemporal chaos, and appear due to potential trapping. By a modal decomposition analysis, we have shown that these states emerge from nonlinear interactions of asymmetric modes. The simple parabolic potential captures the essential dynamics introduced by synchronous phase modulation and permits us to gain useful physical insight.

Funding. European Research Council (740355); H2020 Marie Skłodowska-Curie Actions (101023717, 101064614); Ministero dell'Istruzione, dell'Università e della Ricerca (R18SPB8227).

Disclosures. The authors declare no conflicts of interest.

Data availability. Data underlying the results presented in this paper are not publicly available at this time but may be obtained from the authors upon reasonable request.

REFERENCES

- S. Wabnitz, *Opt. Lett.* **18**, 601 (1993).
- T. Herr, V. Brasch, J. D. Jost, C. Y. Wang, N. M. Kondratiev, M. L. Gorodetsky, and T. J. Kippenberg, *Nat. Photonics* **8**, 145 (2014).
- A. Pasquazi, M. Peccianti, L. Razzari, D. J. Moss, S. Coen, M. Erkintalo, Y. K. Chembo, T. Hansson, S. Wabnitz, P. Del'Haye, X. Xue, A. M. Weiner, and R. Morandotti, *Phys. Rep.* **729**, 1 (2018).
- M. Haelterman, S. Trillo, and S. Wabnitz, *Opt. Commun.* **91**, 401 (1992).
- Y. K. Chembo, D. Gomila, M. Tlidi, and C. R. Menyuk, *Eur. Phys. J. D* **71**, 299 (2017).
- P. Parra-Rivas, E. Knobloch, D. Gomila, and L. Gelens, *Phys. Rev. A* **93**, 063839 (2016).
- P. Parra-Rivas, D. Gomila, L. Gelens, and E. Knobloch, *Phys. Rev. E* **97**, 042204 (2018).
- P. Parra-Rivas, E. Knobloch, L. Gelens, and D. Gomila, *IMA J. Appl. Math.* **86**, 856 (2021).
- F. Leo, S. Coen, P. Kockaert, S.-P. Gorza, P. Emplit, and M. Haelterman, *Nat. Photonics* **4**, 471 (2010).
- M. Anderson, F. Leo, S. Coen, M. Erkintalo, and S. G. Murdoch, *Optica* **3**, 1071 (2016).
- Z. Liu, M. Ouali, S. Coulibaly, M. G. Clerc, M. Taki, and M. Tlidi, *Opt. Lett.* **42**, 1063 (2017).
- E. Lucas, M. Karpov, H. Guo, M. L. Gorodetsky, and T. J. Kippenberg, *Nat. Commun.* **8**, 736 (2017).
- C. Bao, Y. Xuan, C. Wang, A. Fülöp, D. E. Leaird, V. Torres-Company, M. Qi, and A. M. Weiner, *Phys. Rev. Lett.* **121**, 257401 (2018).
- C. Milán and D. V. Skryabin, *Opt. Express* **22**, 3732 (2014).
- P. Parra-Rivas, D. Gomila, F. Leo, S. Coen, and L. Gelens, *Opt. Lett.* **39**, 2971 (2014).
- M. Tlidi and L. Gelens, *Opt. Lett.* **35**, 306 (2010).
- P. Parra-Rivas, D. Gomila, and L. Gelens, *Phys. Rev. A* **95**, 053863 (2017).
- Z. Li, Y. Xu, S. Coen, S. G. Murdoch, and M. Erkintalo, *Optica* **7**, 1195 (2020).
- P. Parra-Rivas, S. Coulibaly, M. Clerc, and M. Tlidi, *Phys. Rev. A* **103**, 013507 (2021).
- S. Wabnitz, *J. Opt. Soc. Am. B* **13**, 2739 (1996).
- J. K. Jang, M. Erkintalo, S. Coen, and S. G. Murdoch, *Nat. Commun.* **6**, 7370 (2015).
- D. C. Cole, J. R. Stone, M. Erkintalo, K. Y. Yang, X. Yi, K. J. Vahala, and S. B. Papp, *Optica* **5**, 1304 (2018).
- I. Hendry, B. Garbin, S. G. Murdoch, S. Coen, and M. Erkintalo, *Phys. Rev. A* **100**, 023829 (2019).
- F. R. Talenti, T. Hansson, and S. Wabnitz, *Advanced Photonics Congress 2020* (2020), p. JT2D.4.
- M. Erkintalo, S. G. Murdoch, and S. Coen, *J. R. Soc. N. Z.* **52**, 149 (2022).
- A. Mecozzi, J. D. Moores, H. A. Haus, and Y. Lai, *J. Opt. Soc. Am. B* **9**, 1350 (1992).
- N. Englebert, N. Goldman, M. Erkintalo, N. Mostaan, S.-P. Gorza, F. Leo, and J. Fatome, "Bloch oscillations of driven dissipative solitons in a synthetic dimension," *arXiv*, arXiv:2112.10756 (2021).
- A. K. Tusnín, A. M. Tikan, and T. J. Kippenberg, *Phys. Rev. A* **102**, 023518 (2020).
- V. E. Lobanov, G. V. Lihachev, N. G. Pavlov, A. V. Cherenkov, T. J. Kippenberg, and M. L. Gorodetsky, *Opt. Express* **24**, 27382 (2016).
- A. U. Nielsen, Y. Xu, C. Todd, M. Ferré, M. G. Clerc, S. Coen, S. G. Murdoch, and M. Erkintalo, *Phys. Rev. Lett.* **127**, 123901 (2021).
- H. Taheri, A. A. Eftekhari, K. Wiesenfeld, and A. Adibi, *IEEE Photonics J.* **7**, 1 (2015).
- N. Verschuere, U. Bortolozzo, M. G. Clerc, and S. Residori, *Phil. Trans. R. Soc. A* **372**, 20140011 (2014).
- K. Krupa, A. Tonello, A. Barthélémy, T. Mansuryan, V. Couderc, G. Millot, P. Grelu, D. Modotto, S. A. Babin, and S. Wabnitz, *APL Photonics* **4**, 110901 (2019).
- M. Haelterman, S. Trillo, and S. Wabnitz, *Opt. Commun.* **93**, 343 (1992).
- E. J. Doedel, "AUTO-07p: continuation and bifurcation software for ordinary differential equations," Dept. Comput. Sci. Concordia Univ. Montr. (2007).
- F. Leo, L. Gelens, P. Emplit, M. Haelterman, and S. Coen, *Opt. Express* **21**, 9180 (2013).
- Y. Sun, S. Combrié, F. Bretenaker, and A. D. Rossi, *Phys. Rev. Lett.* **123**, 233901 (2019).
- Y. Sun, S. Combrié, A. D. Rossi, and F. Bretenaker, *Phys. Rev. A* **102**, 043503 (2020).